Available online at www.sciencedirect.com

ScienceDirect

Underground Space 3 (2018) 125–139

www.elsevier.com/locate/undsp

3D finite element modelling optimization for deep tunnels with material nonlinearity

Osvaldo P.M. Vitali [a,*], Tarcisio B. Celestino [b], Antonio Bobet [a]

[a] *Lyles School of Civil Engineering, Purdue University, West Lafayette, IN 47907, USA*
[b] *Sao Carlos School of Engineering, Univerity of Sao Paulo, Sao Carlos, SP 13566, Brazil*

Received 18 September 2017; received in revised form 16 November 2017; accepted 19 November 2017
Available online 28 November 2017

Abstract

3D modeling of tunnels using a nonlinear ground model is still a time-consuming task because it usually requires a large number of incremental phases with iterative processes, to ensure accuracy while minimizing computational effort. Optimization of the finite element mesh is of utmost importance. Despite the current tendency towards 3D modeling of tunnels, few publications are concerned with mesh optimization considering model size, grid refinement and order of elements. This paper improves the understanding of key issues that affect 3D modeling of tunnels. Our results shown that: (1) 2nd order elements are more efficient when material nonlinearity is present and should be preferred; (2) the plastic zone size has a strong influence on the model dimensions and may require discretizations much larger than those currently accepted. The paper provides recommendations for mesh refinement and model dimensions (width and length) as a function of the plastic zone size, for accurate 3D models with reduced computational cost.

Keywords: Tunnel; Numerical modeling; Finite element method; Mesh optimization; Nonlinear material

Introduction

Tunnel design currently relies on numerical models thanks to the increase of computer capabilities, together with the development of sophisticated and user-friendly finite element codes and ground models. The 3D modeling of tunnels is becoming more attractive due to recognized limitations of the 2D modeling (Janin et al., 2015; Möller, 2006), and because 3D modelling is able to capture better the response of tunnel excavations (Janin et al., 2015; Mašín, 2009; Möller, 2006; Svoboda & Masin, 2011; Yeo et al., 2009).

Despite the improvements in hardware and software, 3D modelling of tunnels is still a time-consuming task because it involves incremental phases to simulate the excavation and, most often, incorporates material nonlinearity (i.e. plasticity). The step-by-step excavation procedure consists of a sequence of phases where the elements inside the opening (excavation rounds) are deactivated while the elements that represent the liner are activated.

The potentially large number of incremental phases, complemented with material nonlinearity (i.e. several iterations to converge), makes the 3D modelling of tunnels expensive. For instance, Franzius & Potts, 2005 mentioned calculation times of 291.3 h to run a 45,947 nodes finite element model with 40 incremental phases and 194.9 h to run a 38,083 nodes model with 32 incremental phases on a Sun SF 880 server at Cambridge University. They also suggested that the excavation round length used in the model should be linked to the computational capabilities, given that this parameter strongly influences the time for processing.

* Corresponding author.
E-mail address: ovitali@purdue.edu (O.P.M. Vitali).

https://doi.org/10.1016/j.undsp.2017.11.002

More recently, Do, Dias, Oreste, & Djeran-Maigre, 2014, performed a 3D numerical study of mechanized twin tunnels simulating details of the excavation, such as face pressure, shield weight and gap filled with grouting. Their models had 1,100,000 nodes and required 340 h (approx. 2 weeks) to run using a 2.67 GHz core i7 CPU RAM 24G computer. Despite improvements of hardware, tunnel models are increasing in complexity and, therefore, requiring more computational effort to run. Such effort may make 3D modelling unfeasible for some applications. An optimum finite element mesh that leads to accurate results in reasonable time is necessary to make 3D modelling feasible, for both industry and research. Surprisingly, few publications on numerical modelling of tunnels are dedicated to mesh optimization.

The literature presents a wide range of model sizes (length and width) and finite element grids (Do et al., 2014; Eberhardt, 2001; Gomes & Celestino, 2009; Janin et al., 2015; Möller, 2006; Nam & Bobet, 2007; Ng & Lee, 2005; Svoboda & Masin, 2011; Yeo et al., 2009), that seem to indicate that there is no well-stablished procedure to define model dimensions and grid refinement. For instance, Franzius & Potts, 2005, summarized the model dimensions carried out by other authors. From the summary, one can observe that the model width has an average of $17.8R_{tunnel}$ and a standard deviation of $10R_{tunnel}$ (R_{tunnel} is the radius of the tunnel); and the model length has an average of $27.2R_{tunnel}$ and a standard deviation of $15.2R_{tunnel}$. These statistics illustrate the large scatter of the models sizes found in the literature.

Most of the recommendations for model size consider stresses, strains and displacements at the boundaries. Meisnerr, 1996, cited by Möller, 2006, states that a $8R_{tunnel}$ to $10R_{tunnel}$ model width would be enough to minimize errors; this is in agreement with the rule of thumb that the boundaries should be at least $10R_{tunnel}$ far from the opening. However, such recommendation suggests that the boundaries are only affected by the size of the tunnel and not by other variables such as the initial stresses, plastic size and/or geological features.

Möller, 2006, proposed expressions to establish the model dimensions for shallow tunnels as a function of the tunnel diameter and the overburden ratio (ratio between tunnel depth and tunnel radius), by using an advanced constitutive model for the ground (a hardening soil model), while considering surface settlements and shear stress mobilization at the boundaries. The criteria were that the settlement at a lateral boundary should not exceed 1% of the maximum settlement along the surface and that the principal stress directions should not rotate more than 2.5° with respect to their initial directions at the boundaries. Such limits are uncertain and do not provide information on the accuracy achieved by the numerical model around the opening; also, the conclusions did not explicitly consider the size of the plastic zone. Interestingly, Möller, 2006, found that the necessary mesh width was the same for 2D and 3D models.

Vlachopoulos & Diederichs, 2014, recommended that the boundaries should be placed at least 12 tunnel radius (R_{tunnel}) from the opening and at least $3R_{yield}$ (yield radii) from the plastic zone around the opening. However, no relation was provided between the size of the model and the accuracy achieved around the opening, nor the criteria for the recommendation.

This paper seeks to improve our understanding on how the finite element mesh and the sequential excavation modelling affect the numerical results, considering material nonlinearity; thus, providing guidelines and information for practitioners and academicians to build more efficient and reliable 3D models.

Grid refinement and type of element

3D models of tunnels are usually built by extruding a 2D grid along the tunnel axis. All references consulted (except Janin et al., 2015, which adopted a 3D mesh with tetrahedron elements) used extrusion. Figure 1 illustrates the most common type of 3D models found in the literature.

The aim of this section is to investigate the transversal grid refinement and the order of the elements (i.e. interpolation function) for 3D simulations.

Grid refinement and order of elements were evaluated such that nonlinear behavior was accurately captured; that is, the goal was to find whether there is an advantage of using quadratic interpolation elements (serendipity 2nd order elements – 20 node hexahedron elements) instead of linear interpolation elements (1st order elements – 8-node hexahedron elements) and how refined the grid should be to obtain accurate results.

Numerical accuracy, defined as how close a result is from its true value, was assessed using the results obtained with a very refined grid. Fig. 2 shows a cross section perpendicular to the tunnel axis, far from the face such that uniform results are obtained. The numerical output is consistent with the analytical solution developed for plane strain hollow plates loaded at the boundaries, for elastic perfectly plastic Mohr-Coulomb material (Salesçon, 1969). Such analytical solution has been used to validate the elastic perfectly plastic Mohr-Coulomb model in FEM codes, such as Midas NX GTS (MIDAS Information Technology Co., 2014). More specifically, comparisons are made with the radial displacements at the perimeter of the opening.

Accuracy is calculated using the following equation, which measures the error between the true (reference) solution and the value obtained from a given realization.

$$Accuracy\ (\%) = \frac{|u - u_{reference}|}{|u_{reference}|}$$

where $u_{reference}$ is taken from the reference mesh. Note that the accuracy is expressed as a percentage.

A deep unsupported circular tunnel is assumed, with a radius of 5 m ($R_{tunnel} = 5$ m), subjected to far-field

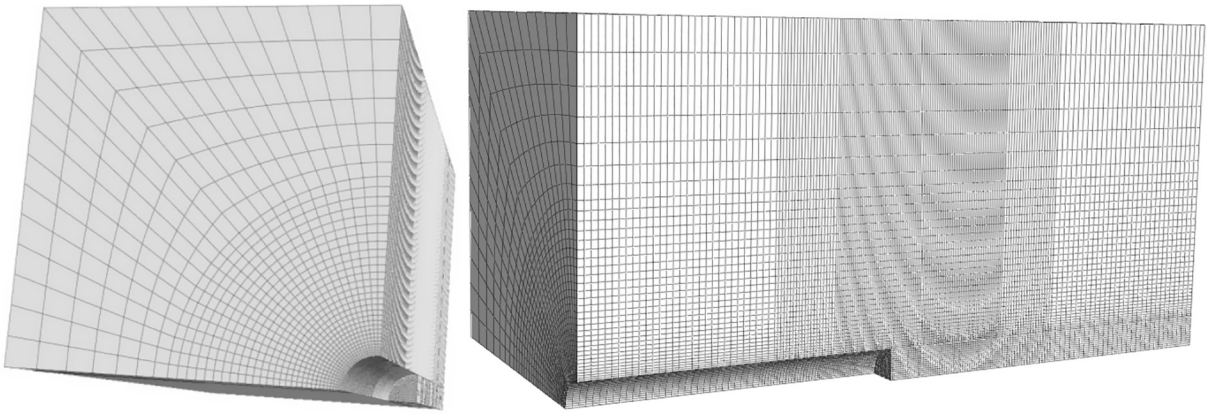

Fig. 1. Typical 3D tunnel model found in the literature, typically built by extrusion of a 2D grid.

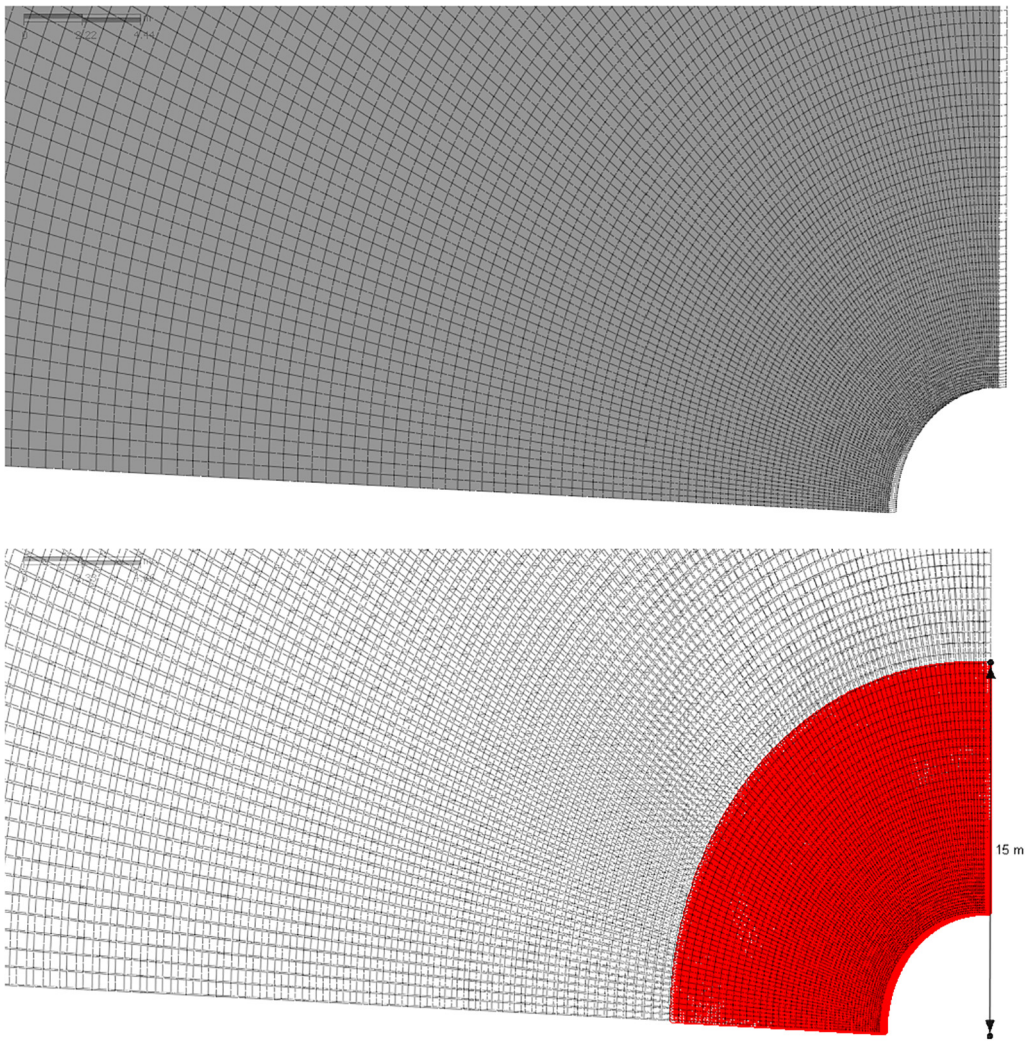

Fig. 2. Refined mesh using 2nd order hexahedra, used as reference, and yield ground.

geostatic pressures of 100 kPa and coefficient of earth pressure at rest, K_o, equal to 1, i.e. hydrostatic loading. Note that under these conditions, the problem has axial symmetry. It is common practice to adopt a uniform stress field with depth for deep tunnel analysis. This is a valid assumption because the changes in stress with depth are negligible for a deep tunnel (Bobet, 2003). For the models, the lateral boundaries are placed at 250 m ($50R_{tunnel}$) from the center of the tunnel, a distance large enough such that errors due to the boundaries are avoided, and the axial

boundaries are also far enough such that plane strain conditions are achieved at the cross section of interest.

The ground models were either linear elastic ($R_{yield} = R_{tunnel}$) or elastic perfectly plastic with a Mohr-Coulomb failure with associated flow rule ($\Psi = \phi = 19.6°$), that results in $R_{yield} = 3R_{tunnel}$ (the soil properties are presented in Table 1). Note that a yield radius greater than three times the tunnel radius is unlikely in practice because it would lead to unacceptable ground movements and even collapse of the opening. In weak ground conditions, the support would prevent such large plastic deformations around the opening. Therefore, $R_{yield} = 3R_{tunnel}$ is representative of the worst case scenario. Further, an associated flow rule was assumed, which carries relatively high volumetric plastic strains ($\Psi = \phi = 19.6°$), making the material nonlinearity more noticeable.

Figure 2 shows the refined mesh with 2nd order elements, used as Ref. Fig. 2 also shows the yield radius obtained using the parameters presented in Table 1 for $R_{yield} = 3R_{tunnel} = 15$ m. The size of the yield radius matches the analytical solution.

The strength parameters shown in Table 1 (cohesion and friction angle) were determined given the yield radius (R_{yield}) for 100 kPa hydrostatic pressure, using Salesçon's solution. The size of the plastic zone is representative of the level of nonlinearity of the numerical model. Therefore, the recommendations throughout the paper may be applicable to other ground conditions, far-field stresses and to supported tunnels, based on the size of the plastic zone developed around the tunnel.

Both structured and unstructured grids are investigated. Structured grids have a regular pattern, and are common in the literature (Eberhardt, 2001; Gomes & Celestino, 2009; Nam & Bobet, 2007; Nicholas Vlachopoulos & Diederichs, 2014). Unstructured grids have an irregular pattern. Unstructured grids provide more flexibility to discretize the domain compared to structured grids, given that they allow complex nodal connectivity and different element types (i.e. rectangular and triangular elements). Therefore, initially, unstructured grids could be preferable because they allow a more efficient distribution of nodes and quadrature points; that is, a more refined grid in the region near the opening and a coarser grid far from the opening.

First, structured grids are analyzed. A total of 6 different grids are assessed. The grids are made by dividing the opening perimeter and the boundaries equally, adopting a refined grid close to the opening that gradually coarsens towards the boundaries.

Table 1
Soil properties for R_{yield}/R_{tunnel} ratios. Tunnel with $R_{tunnel} = 5$ m and 100 kPa far-field hydrostatic pressure.

R_{yield}/R_{tunnel}	c (kPa)	ϕ (°)	E (MPa)	ν
1	–	–	100	0.3
1.5	28.1	19.6	100	0.3
2	17.5	19.6	100	0.3
2.5	12.7	19.6	100	0.3
3	10.0	19.6	100	0.3

Figure 3 plots the normalized radial displacement at the perimeter of the opening, as a function of the number of nodes of the different grids. The radial displacements are normalized by those of the reference model (Fig. 2) using the same ground properties. The computational effort is directly related to the number of nodes, which determines the size of the system of equations to be solved, while the efficiency of a model relates the accuracy achieved with the number of nodes in the model; that is, the higher the accuracy and the smaller the number of nodes, the more efficient the mesh is. Thus, the efficiency of the finite element mesh can be assessed by comparing the number of nodes with the accuracy achieved.

Figure 3 shows that, for all cases analyzed, the difference in normalized displacements from the case considered "correct" decreases as the number of nodes (i.e. as the number of elements) increases. It is interesting to note that irrespective of the type of element, either first order or second order, the errors are small if the ground model is elastic. This is not the case however when plasticity is considered. Indeed, when the material yields ($R_{yield} = 3R_{tunnel}$ and associated flow rule, $\Psi = \phi = 19.6°$), the most refined mesh with 1st order elements achieves a 12.8% accuracy using 918 nodes, while the coarser mesh with 2nd order elements achieves a 4.9% accuracy using only 287 nodes. The grid with 2nd order elements considered optimum (coarsest grid with errors smaller than 1% for nonlinear material) is presented in Fig. 4. In this case, the errors are 0.6% with 836 nodes.

The data in Fig. 3 show that 2nd order elements are more efficient than 1st order elements, when material nonlinearity is present. This observation can be explained because of the quadratic interpolation of the 2nd order elements that can capture the nonlinear material behavior

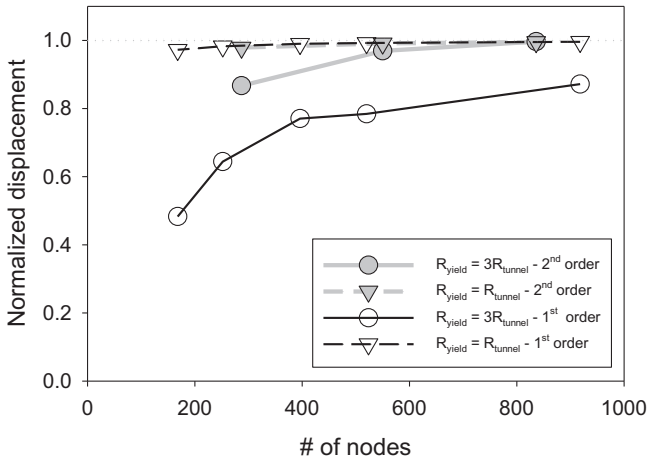

Fig. 3. Convergence towards reference radial displacement for structured grid with 1st order and 2nd order elements (8-nodes and 20-nodes hexahedral elements).

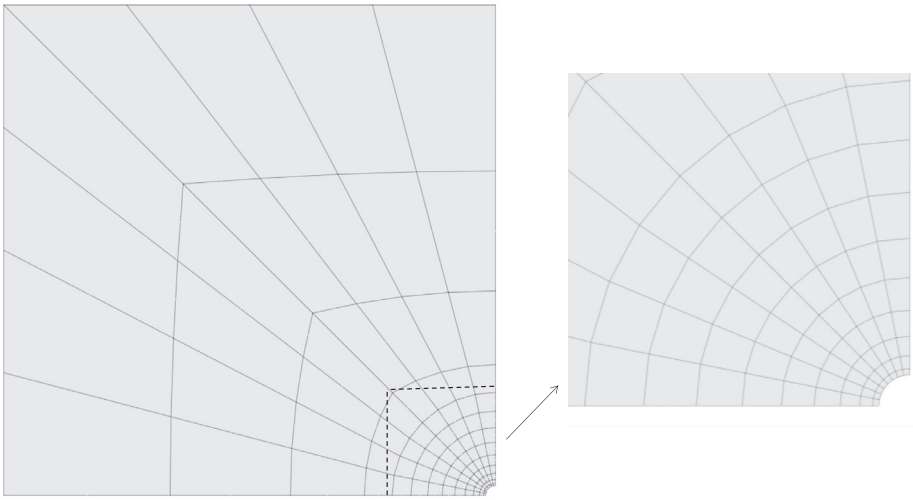

Fig. 4. Front view of the optimum structured grid with 2nd order elements.

more accurately than the linear interpolation of 1st order elements. This conclusion is strengthened by the fact that, for linear material ($R_{yield} = R_{tunnel}$), there is no advantage in using 2nd order elements over 1st order elements.

To assess the influence of the grid pattern, three types of grids using 2nd order elements with approximately the same number of nodes are compared: (1) structured grid using hexahedron elements; (2) unstructured grid using only pentahedron elements (grid A); and (3) unstructured grid using hexahedron and pentahedron elements (grid B). The grids are developed using a mesh generator with Delaunay algorithm with a refined mesh close to the opening that gradually coarsens toward the boundary.

Similar to Fig. 3, Fig. 5 compares the radial displacements at the perimeter of the opening, normalized with respect to the reference model displacements (Fig. 2), for different types of grid and number of nodes. Results are obtained for nonlinear material ($R_{yield} = 3R_{tunnel}$ and associated flow rule, see Table 1). As expected, as the number of nodes in the discretization increases, e.g. as the number of elements increase, the errors decrease and the solution converges towards the correct solution. The three types of grids provide similar accuracy for the same number of nodes. Therefore, the type of the grid structure is not as important as the type of element. Figs. 6 and 7 show the optimum unstructured grids. Grid A, with pentahedron elements only, has 724 nodes and achieves 0.8% accuracy, while grid B, with hexahedron and pentahedron elements, has 589 nodes and 1% accuracy.

Despite the advantage of using 2nd order elements (i.e. quadratic interpolation), with respect to 1st order elements, models are found in the literature that use 1st order elements (i.e. linear interpolation). For instance, Ng & Lee, 2005, used 1st order elements due to limitations of computational resources; however, it is arguable that a faster mesh resulting in equally or better results is possible using a coarser grid with 2nd order elements, based on the results presented in this paper.

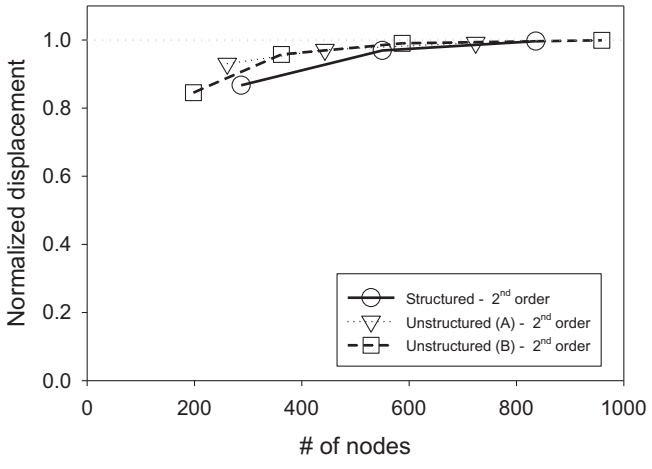

Fig. 5. Convergence towards reference radial displacement for different types of grid with 2nd order elements.

3D mesh dimensions

Mesh width

The influence of the model width on the accuracy of the results was assessed by a set of analyses varying the model width (L_{width}) and the degree of material nonlinearity (yield radius ranging from 1 to 3 times the tunnel radius; see soil properties in Table 1). Examples of the meshes investigated are presented in Fig. 8 (only the front face is shown, for clarity). Similar to previous examples, the tunnel radius is 5 m and the stress state is hydrostatic (i.e. $K_0 = 1$), with far field stress 100 kPa.

As discussed, the range of model widths found in the literature is high, from $48.2R_{tunnel}$ to $8R_{tunnel}$ (Franzius & Potts, 2005). Also, there is no well-established procedure to determine the model width. Further, most of the

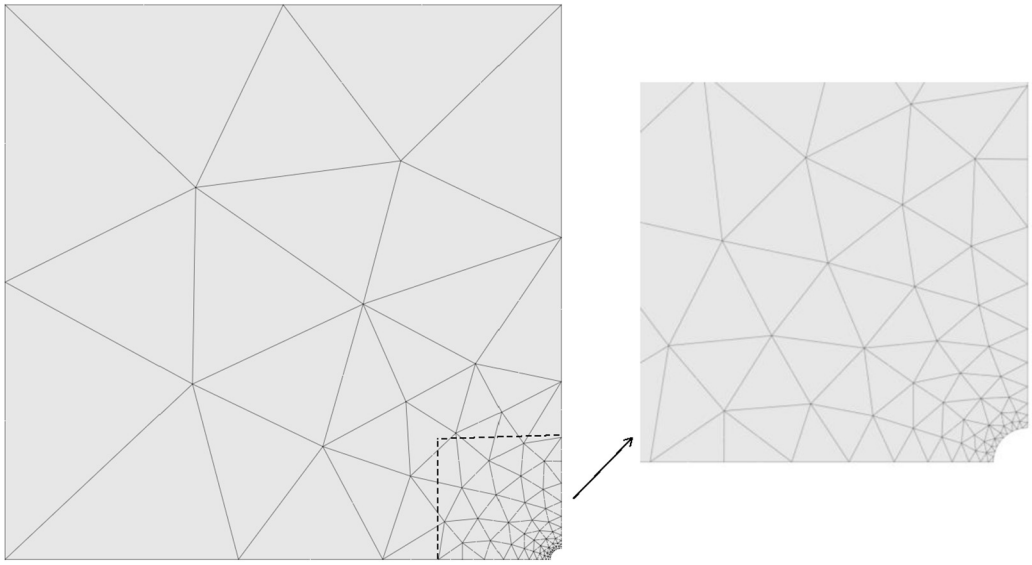

Fig. 6. Front view of the optimum unstructured grid A with 2nd order elements.

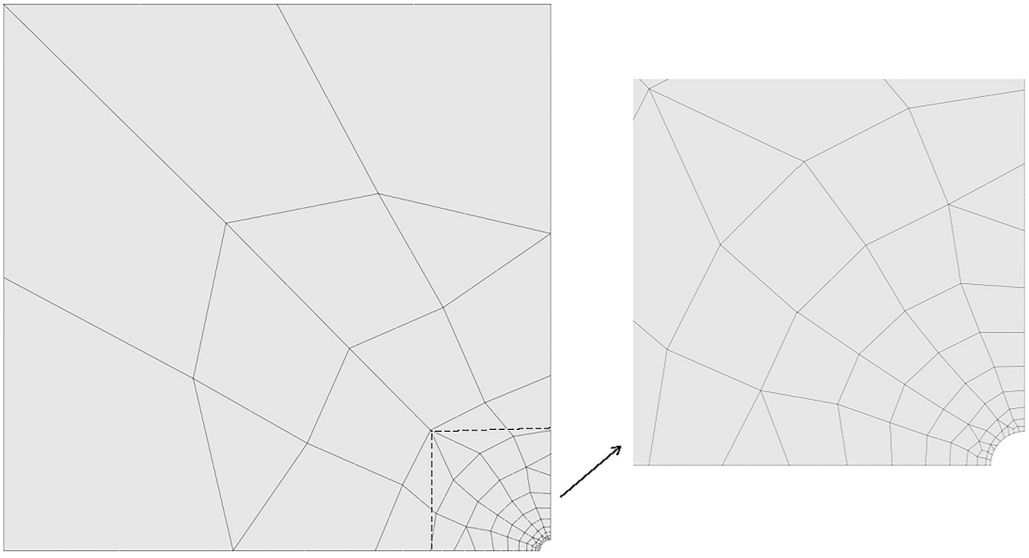

Fig. 7. Front view of the optimum unstructured grid B with 2nd order elements.

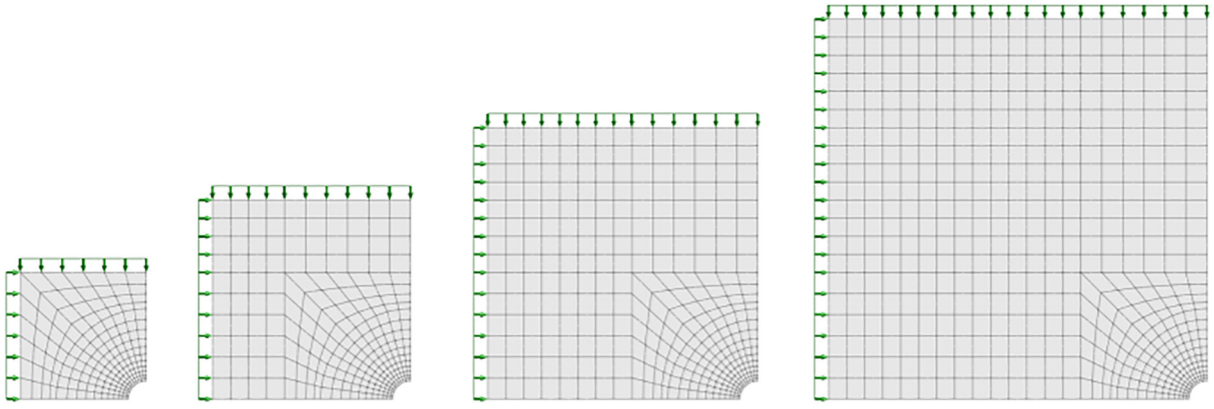

Fig. 8. Examples of the front view of finite element meshes with 2nd order elements (20-node hexahedra) to assess the influence of model width. Note that the grid refinement is kept constant regardless of the mesh size.

suggestions found often do not account for important aspects such as the size of the plastic zone and there are no recommendations relating mesh size and accuracy.

Figure 9 plots the error of the radial displacements at the perimeter of the opening with respect to the reference value, which is the displacement obtained numerically with a model extremely wide ($200R_{tunnel}$), using the grid structure shown in Fig. 8. The figure shows that the errors quickly decrease as the width of the mesh increases. The figure also shows that, as the size of the plastic zone around the tunnel increases, the errors increase.

It is interesting to see that the errors are smaller than 5% for mesh widths larger than about 15 times the tunnel radius and become negligible for widths larger than 40–45 tunnel radius. It is worth noting that, for a model width equal to $10R_{tunnel}$, which is a common reference in the literature (Möller, 2006), the error is acceptable for linear elasticity (1.3%), but may be unacceptable for $R_{yield} = 3R_{tunnel}$ (13%). Also, the Vlachopoulos & Diederichs, 2014, recommendation to adopt a model size of $3R_{yield}$ beyond the plastic zone may lead to inaccurate results. For instance, for $R_{yield} = 3R_{tunnel}$, the criterion requires a model size of $12R_{tunnel}$, which would result in an error of 8.5%, according to Fig. 9.

Figure 10 shows the required model width (L_{width}), as a function of the yield radius, to obtain errors below 2%, 1% and 0.5%. For a given accuracy, the width of the mesh needed increases with the size of the plastic zone. These observations, however, apply for the case of isotropic stress field, which results in a yield zone that has axial symmetry. In general, the far-field stresses are anisotropic, and so the plastic zone around the tunnel will not be cylindrical. In this case, the recommendation is to adopt the largest plastic zone size, measured from the center of the opening. This is discussed in more detail in Secti on 'Conclusions', where a case with anisotropic stress field is analyzed.

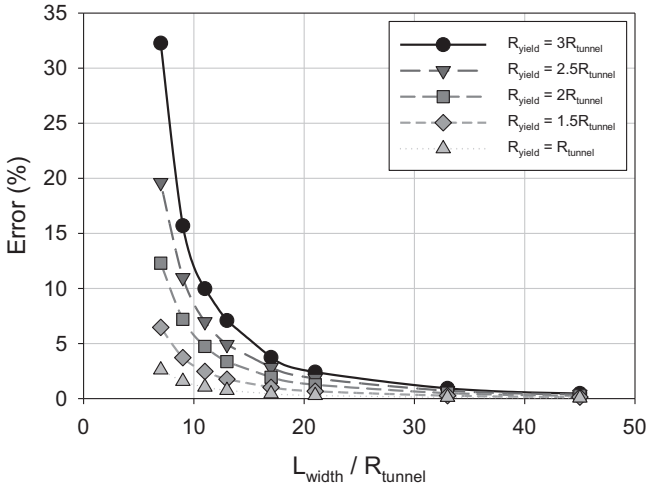

Fig. 9. Relation between accuracy, model width (L_{width}) and plastic radius (R_{yield}).

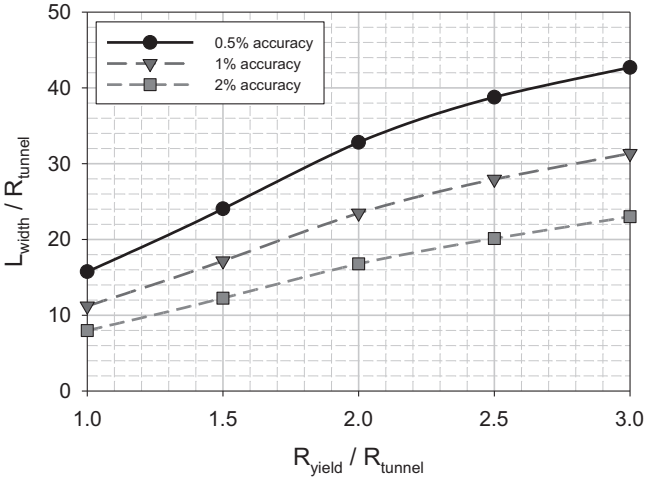

Fig. 10. Model width and accuracy with plastic radius.

Mesh length

The model must be long enough to capture the changes of stresses and displacements ahead and behind the excavation face of the tunnel, without any undesirable effects due to the boundaries. To do this, it is necessary to determine the influence length of the tunnel face; that is, the distance ahead and behind the tunnel face affected by the excavation. Also, it is necessary to assess the influence of the front and back boundaries on the results, such that the solution is free from boundary effects. The goal is to find the minimum model length that accurately captures the 3D tunnel excavation.

As mentioned before, there is no well-established procedure in the literature to estimate the model length. In fact, most of the recommendations disregard the influence of material nonlinearity and do not relate model length with accuracy.

Tunnel face effects

The tunnel excavation changes the stresses in the ground, mobilizing shear stresses (longitudinal and transversal arching) to achieve a new stress state. This process is gradual, starts with the initial stresses in the ground and ends up with a steady-state response at some distance behind the face of the tunnel.

It is informative to determine the location where the stresses in the ground start to be affected by the tunnel excavation and where the displacements stop changing behind the tunnel face; in other words, to determine the length of influence of the tunnel face, which can be done by assessing the displacements and stresses evolution along the tunnel.

A model with $80R_{tunnel}$ length and $50R_{tunnel}$ width using a suitable grid with 2nd order elements is built for the analyses (Fig. 11). The length of $80R_{tunnel}$ is large enough to capture the evolution of stresses and displacements along

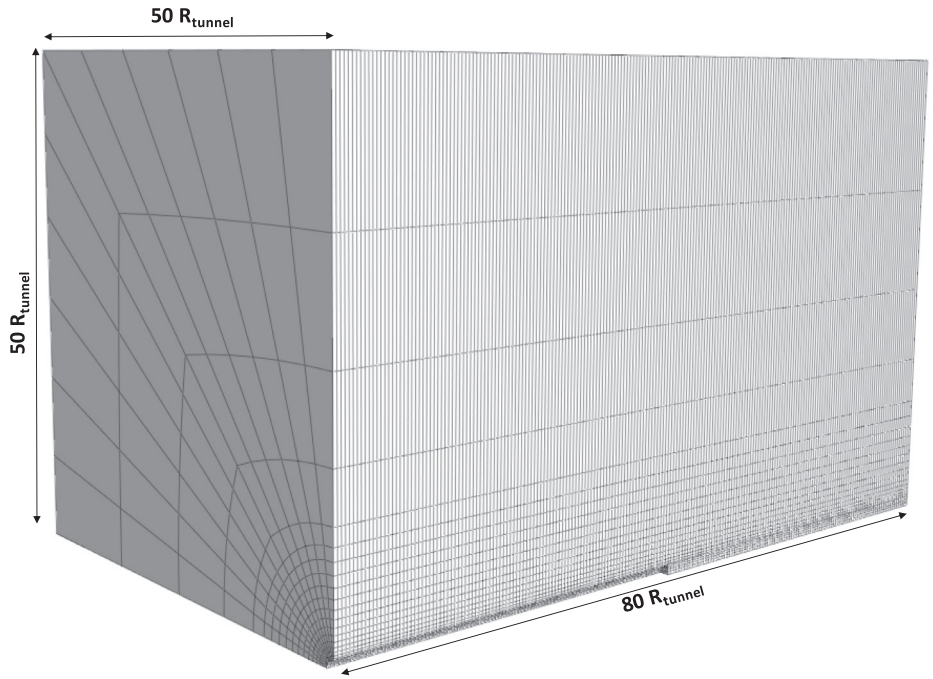

Fig. 11. 3D model using 2nd order elements to assess the length of influence of the tunnel face.

the excavation and avoid boundary effects. Also, the $50R_{tunnel}$ width minimizes boundary effects (see Section 'Mesh width'). The grid refinement and the order of the elements have been discussed in Section 2. In the analyses, the tunnel radius is 5 m and the initial stress state is hydrostatic (i.e. $K_0 = 1$), with a far field stress of 100 kPa. The model has been run for different degrees of material nonlinearity (yield radius ranging from 1 to 3 times the tunnel radius with associated flow rule; see parameters in Table 1).

Möller, 2006, found that the mesh length is almost independent of the excavation round length using a hardening elastoplastic model; therefore, the stress path history due to a step-by-step simulation of the excavation should have a small influence on the model length. Such finding is confirmed by comparing the radial displacement profile obtained with a step by step excavation with a round length of $0.2R_{tunnel}$ and with a single step until the center of the model ($40R_{tunnel}$ long), as will be shown and discussed later in Fig. 12. Therefore, to assess the influence length of the tunnel face, the excavation is simulated in a single step $40R_{tunnel}$ long until the center of the model; this is convenient because of faster computation and simple analysis of the data, given that the single step does not produce the "saw-tooth" shaped results associated with the step by step excavation.

Figure 12 shows the total radial displacements at the perimeter of the opening and those radial displacements normalized with respect to the displacements far from the tunnel face (note also that the figure includes results from a step-by-step excavation with a round length of $0.2R_{tunnel}$). The results are plotted as a function of the distance from the tunnel face (D_{face}) normalized by the tunnel radius (R_{tunnel}). Note that $D_{face}/R_{tunnel} = 0$ is the tunnel face, $D_{face}/R_{tunnel} > 0$ represents a distance ahead of the tunnel face and $D_{face}/R_{tunnel} < 0$ behind the tunnel face.

The displacements start to be mobilized relatively close to the face (at around $4R_{tunnel}$ ahead of the face), with the largest changes occurring near the face. At the face ($D_{face} = 0$), the normalized radial displacement is 0.16 for $R_{yield} = 3R_{tunnel}$ and 0.29 for $R_{yield} = R_{tunnel}$, which is consistent with the literature (Vlachopoulos & Diederichs, 2009). The radial displacement shows an abrupt increase just behind the face and a continued increase towards a steady displacement with distance behind the face. This happens at around $15R_{tunnel}$. The shape of the curves, as one can see in the figure, strongly depends on the size of the plastic zone around the tunnel.

Despite the influence of the step-by-step excavation on the total displacements (note that the radial displacement far behind the face increases by 20% with the step by step excavation for $R_{yield} = 3R_{tunnel}$ and associated flow rule, compared with the single step), for the normalized displacements, after a distance of around $4R_{tunnel}$ behind the face, the normalized radial displacements for $R_{yield} = 3R_{tunnel}$ for the step by step and single step match, denoting that both methods give the same results.

Figure 13 shows the tangential stresses ($\sigma_{\theta\theta}$) near the perimeter of the opening, normalized with respect to the initial stresses, with the distance from the face, normalized by the tunnel radius. For a hydrostatic far-field stress ($\sigma_{11} = \sigma_{22} = \sigma_{33} = p$), the normalized stress is $\sigma_{\theta\theta}/p$. Far ahead from the excavation face, the stress field is isotropic and of magnitude 100 kPa. As the excavation face approaches, the

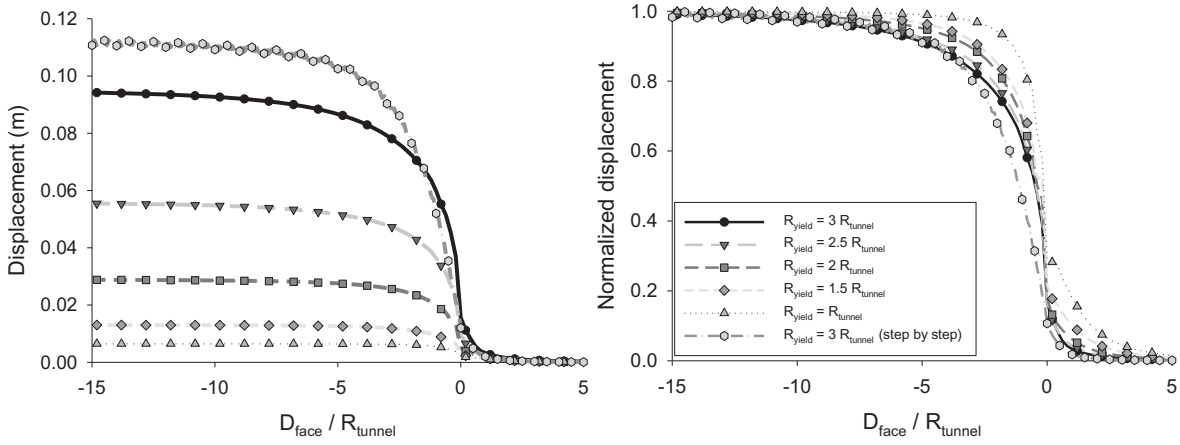

Fig. 12. Radial displacement with distance from the face.

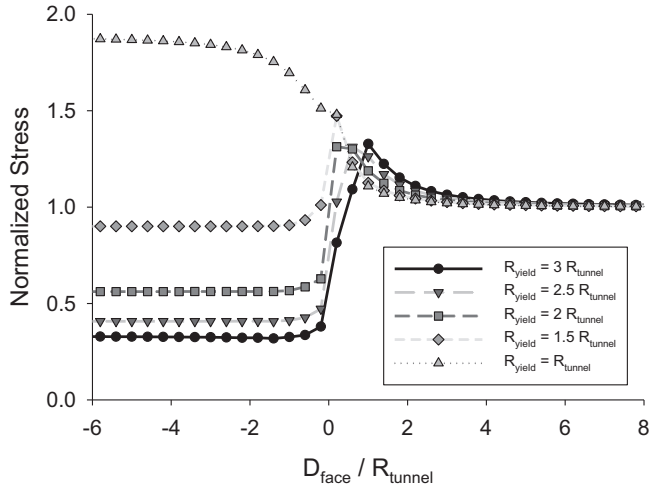

Fig. 13. Tangential stresses near the opening perimeter, with distance from the face.

shear stresses are mobilized (longitudinal and transversal arching) and the tangential stresses start to increase. For a linear elastic material ($R_{yield} = R_{tunnel}$), the tangential stresses monotonically increase until they reach a constant value behind the excavation face. For an elasto-plastic material, yielding limits the increase of the tangential stresses. Once the material yields, the tangential stresses start to decrease until they reach a constant magnitude behind the face, at a distance of around $2R_{tunnel}$. Note that the distance ahead of the face where the shear stresses are mobilized increases with the size of the plastic zone. The stresses shown in Fig. 13 are consistent with Cantieni & Anagnostou, 2009, results for an unsupported tunnel. Note that if a support is installed, an increase in the stresses behind the tunnel face is expected after the support installation, as shown by Cantieni & Anagnostou, 2009.

The length of the model must, at least, extend from the location where stresses or displacements start to be mobilized ahead of the face to where stresses and displacements reach a constant value behind the excavation face; that is, the length must be inclusive of the largest influence of the excavation face.

Figure 14 shows the distance from the tunnel face (D_{face} as multiples of the tunnel radius R_{tunnel}) required to reach an accuracy of 2%, 1% and 0.5%, for tangential stresses and radial displacements, for different sizes of the plastic zone. The plots can be used to estimate the model length, even for models with anisotropic far-field stress, by using the largest size of the yield zone, as it will be shown later in the verification section. Also, the model must include the length affected by the front and back boundaries, as discussed in the next section.

Front and back boundaries

The aim of the section is to determine how results are affected by the front and back boundaries of the model. A model with $20R_{tunnel}$ length and $50R_{tunnel}$ width, with a suitable refined grid, using 2nd order elements is built for the analyses. Figure 15 shows the model. A step-by-step excavation is implemented throughout the entire model to assess the length of influence of the front and back boundaries. As it will be shown, the $20R_{tunnel}$ model length is enough to obtain displacements free from boundary effects.

The model is run for different plastic zone sizes (R_{yield} from 1.5 to 3 R_{tunnel} with associated flow rule, $\psi = \phi = 19.6°$; see input parameters in Table 1), and with an excavation round length of $0.2R_{tunnel}$. Similar to previous discussions, the tunnel radius is 5 m and the stress state hydrostatic (i.e. $K_0 = 1$), with a far field stress of 100 kPa.

Figure 16 shows the radial displacements at the perimeter of the tunnel normalized by the radial displacements far from the influence of the face. The results are plotted as a function of the distance from the center of the model (D_{center}), normalized by the tunnel radius. That is, $D_{center}/R_{tunnel} = 0$ represents the middle of the model; $D_{center}/R_{tunnel} = 10$ represents the back boundary, and $D_{center}/R_{tunnel} = -10$, the front boundary.

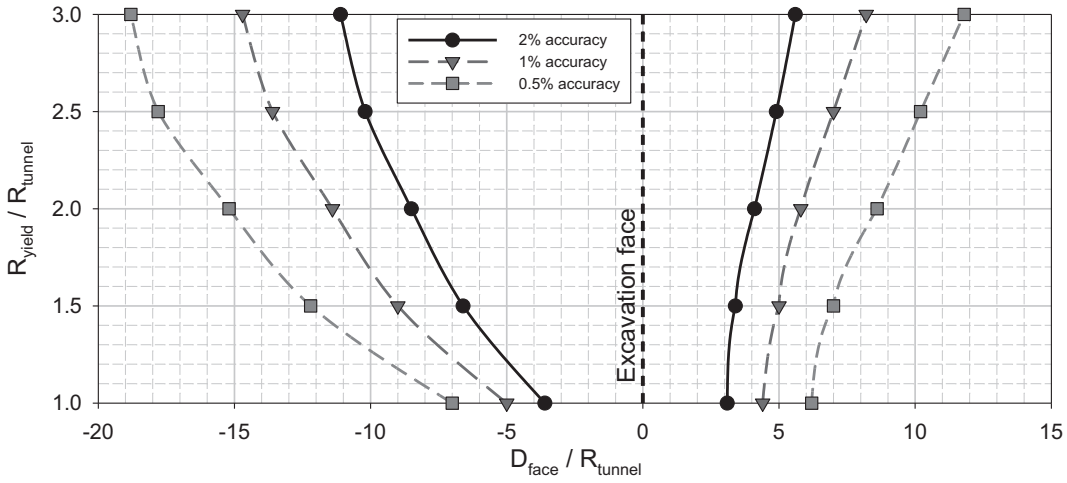

Fig. 14. Minimum distance ahead and behind the tunnel face required to reach a target accuracy, as a function of the plastic zone size.

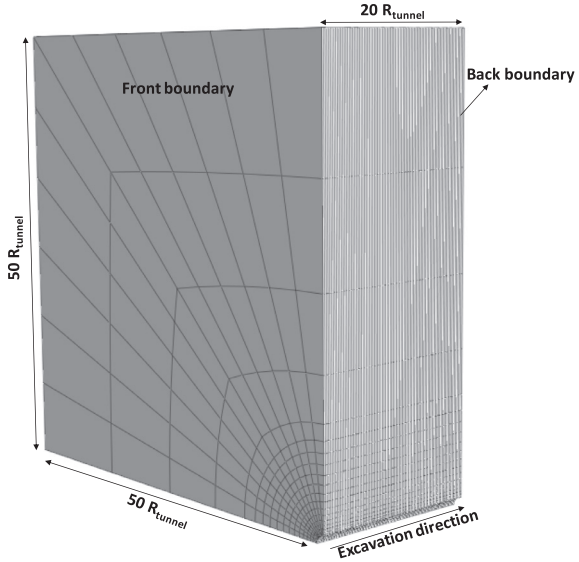

Fig. 15. 3D model to assess the influence of the front and back boundaries.

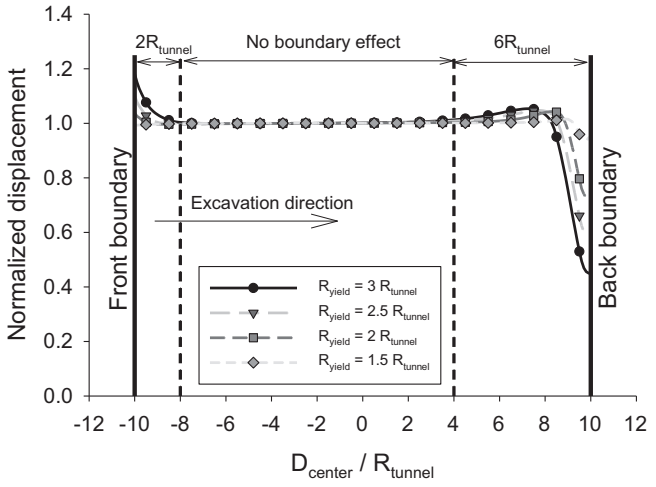

Fig. 16. Normalized radial displacements at the perimeter of the opening, along the tunnel length.

As Fig. 16 shows, the front boundary has an influence over a length of $2R_{tunnel}$ and the back boundary, over $6R_{tunnel}$. It is interesting to note that the length of influence of the front and back boundaries does not vary significantly with the plastic zone size. Thus, in general, results over a length of $2R_{tunnel}$ ahead of the front boundary and $6R_{tunnel}$ behind the back boundary should be disregarded. In other words, any mesh discretization should include an additional $2R_{tunnel}$ length beyond the front boundary and $6R_{tunnel}$ behind the back boundary, to achieve acceptable results.

Axial grid refinement

A 3D tunnel model is usually built by extruding a 2D grid along the tunnel axis. Despite the strong influence that the axial grid refinement has on accuracy and computational effort, as highlighted by Franzius & Potts, 2005, and Möller, 2006, there is limited research on the axial grid refinement. In this section, this issue is discussed.

The models used for this study are similar to those presented in Section 3.2.2 (same dimensions and boundary conditions), but with an excavation round length (L) of $1R_{tunnel}$, $0.4R_{tunnel}$ and $0.2R_{tunnel}$. These values encompass a wide range of excavation round lengths used in practice. The goal is to evaluate the radial displacement profile obtained with the different excavation round lengths, to determine which element length ensures accurate results regardless of the excavation round length. Note that the excavation round length affects the stress path of the ground around the opening; therefore, the radial displacements profile varies with different excavation round lengths, as mentioned by Vlachopoulos & Diederichs, 2009.

Each model is run using different element lengths ($L_{element}$) (i.e. different axial grid refinements). Also, the models are run with $R_{yield} = 3R_{tunnel}$ (see soil properties

in Table 1) and associated flow rule ($\psi = \phi = 19.6°$). Figure 17 shows the models using $L_{element} = 0.1R_{tunnel}$ and $L_{element} = 1R_{tunnel}$.

Figures 18–20 show the radial displacements at the perimeter of the tunnel after excavation throughout the entire model (similar to what was done in Section 3.2.2), shown in Fig. 16, with distance from the center of the model (D_{center}) normalized by the tunnel radius, for excavation round lengths (L) of $1R_{tunnel}$, $0.4R_{tunnel}$ and of $0.2R_{tunnel}$. As before, $D_{center}/R_{tunnel} = 0$ represents the center of the model; $D_{center}/R_{tunnel} = 10$ the back boundary, and $D_{center}/R_{tunnel} = -10$, the front boundary. Those graphs illustrate the influence of the step by step excavation in the displacements, for $R_{yield} = 3R_{tunnel}$ using an elastic perfectly plastic Mohr Coulomb model with associated flow rule. Note that the displacements increase as the excavation round length decreases. For a round length of $0.2R_{tunnel}$, the step by step excavation causes 18% increase of the radial displacements with respect to a single step excavation.

The displacements have the characteristic saw-tooth shape with a periodicity equal to the excavation round. This is a result that has been observed by others (e.g. Möller, 2006). Note also that the amplitude of the saw-tooth, that is the difference between the maximum and minimum displacements, decreases as the round length is reduced; however, the overall magnitude of the displacements increases by decreasing the round length.

For the largest round length, $L = 1R_{tunnel}$, (Fig. 18), the radial displacement profiles obtained for $L_{element} = R_{tunnel}$ (1 element per round) and for $L_{element} = 0.5R_{tunnel}$ (2 elements per round) are inconsistent with the profile obtained using the most refined axial grid ($L_{element} = 0.1R_{tunnel}$). In contrast, the difference between the radial displacements between $L_{element} = 0.2R_{tunnel}$ (5 elements per round) and $L_{element} = 0.1R_{tunnel}$ (10 elements per round) is negligible.

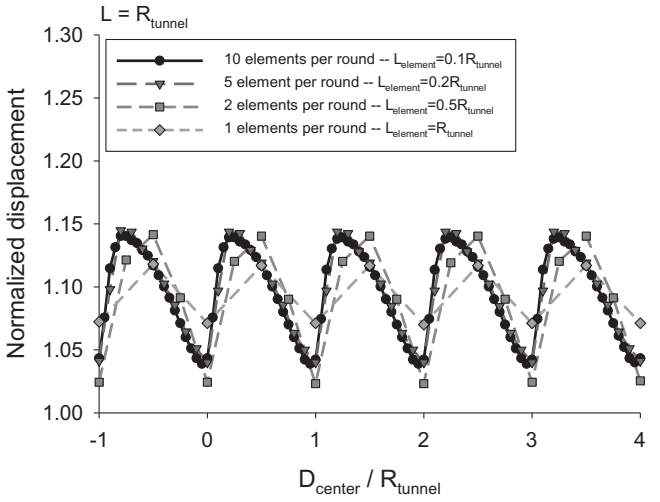

Fig. 18. Radial displacements at the perimeter of the opening along the tunnel length for round lengths (L) of 1 tunnel radius (R_{tunnel}), for different axial grid refinements.

Similarly, for $L = 0.4R_{tunnel}$ (Fig. 19), the radial displacement profiles for $L_{element} = 0.1R_{tunnel}$ and $L_{element} = 0.2R_{tunnel}$ are comparable, but different than $L_{element} = 0.4R_{tunnel}$. Similar observations can be made for $L = 0.2R_{tunnel}$ (Fig. 20). In short, discretization using $L_{element} = 0.2R_{tunnel}$ leads to satisfactory results for all round lengths assessed regardless of the number of

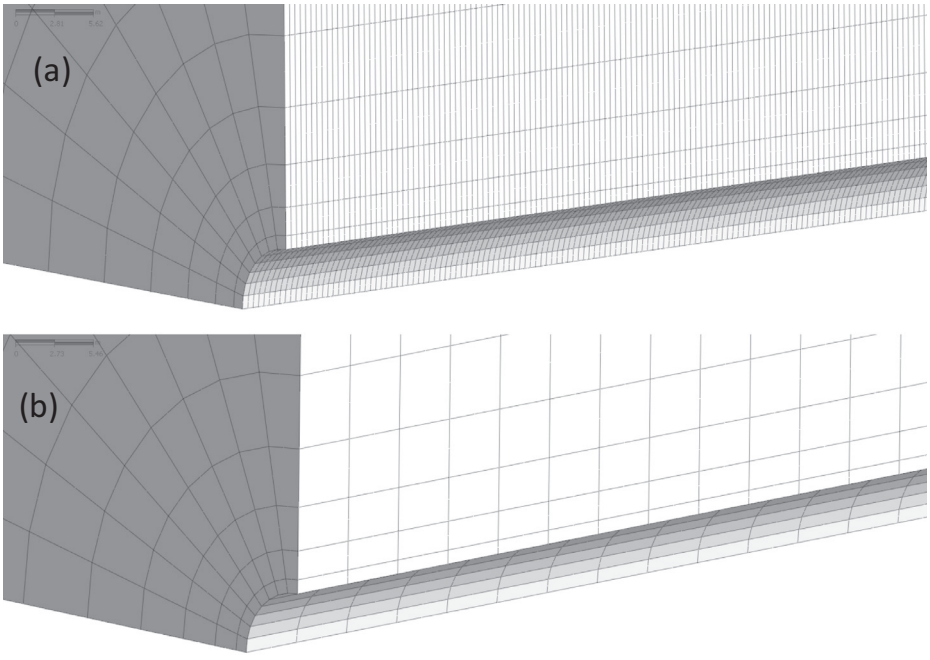

Fig. 17. Models with different axial grid refinement. (a) $L_{element} = 0.1R_{tunnel}$ and (b) $L_{element} = 1R_{tunnel}$.

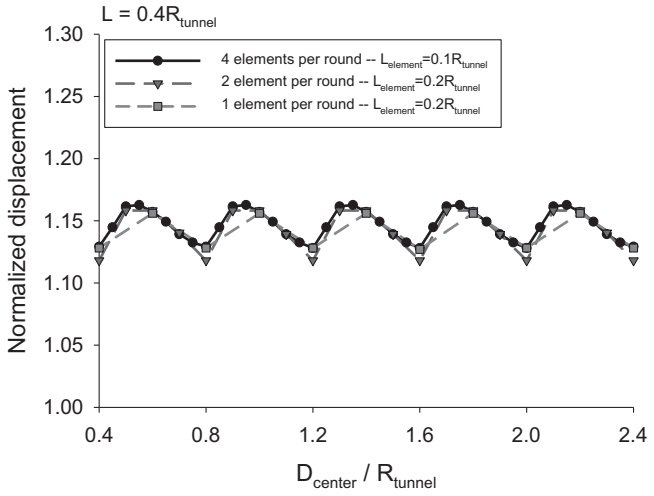

Fig. 19. Radial displacements at the perimeter of the opening along the tunnel length for round lengths (L) of 0.4 tunnel radius (R_{tunnel}), for different axial grid refinements.

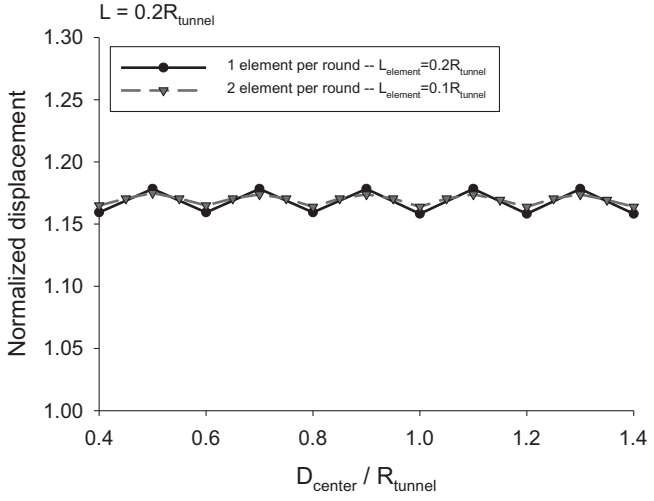

Fig. 20. Radial displacements at the perimeter of the opening along the tunnel length for round lengths (L) of 0.2 tunnel radius (R_{tunnel}), for different axial grid refinement.

elements per round length. Thus, element lengths of $0.2R_{tunnel}$ or shorter seem appropriate for the axial grid, regardless of the excavation round length.

Verification

The previous analyses have been conducted assuming a hydrostatic far-field stress. While the assumption has been useful to identify the critical issues and reach simple conclusions, in reality, the geostatic stresses are anisotropic. It is thus imperative to determine to what extent the observations made can be generalized. To do this, additional analyses are made: a 3D model with large dimensions and refined mesh (reference model) is compared with a 3D model with dimensions and mesh refinement following the recommendations made based on the previous simulations. An excavation round length of 5 m (i.e. one tunnel radius), tunnel radius of 5 m, anisotropic stress field (i.e. $\sigma_1 = 100$ kPa, $\sigma_2 = \sigma_3 = 50$ kPa) and an elastic, perfectly plastic Mohr-Coulomb material with parameters for $R_{yield} = 2R_{tunnel}$ and non-associated flow rule ($\Psi = 0°$) (see Table 1) is adopted. Under such conditions, the shape of the plastic zone around the opening is not circular and the maximum distance from the center of the opening to the limit of the plastic zone is approximately $2R_{tunnel}$.

Figure 21 shows the reference 3D model, which uses 2nd order elements and has $80R_{tunnel}$ length and $50R_{tunnel}$ width. Such dimensions are sufficient to capture the displacements and stresses in the tunnel without boundary effects. The model uses an element length of $0.2R_{tunnel}$ within the volume comprised between $30R_{tunnel}$ behind the excavation face and $20R_{tunnel}$ ahead of the excavation face. The axial grid is coarsened close to the front and back boundaries to save processing time.

Figure 22 shows the grid built following previous recommendations. That is, the model uses 2nd order elements and mesh following Fig. 4; the model width is $25R_{tunnel}$, based on Fig. 10 (assuming a 1% accuracy and $R_{yield} = 2R_{tunnel}$); the model length is $26R_{tunnel}$, based on Figs. 14 and 16 (assuming 1% accuracy and $R_{yield} = 2R_{tunnel}$; $12R_{tunnel}$ behind the face and $6R_{tunnel}$ ahead of the face); and the element length is $0.2R_{tunnel}$, as discussed in Section 4.

Figure 23 shows the radial displacements obtained from both models along the axis of the tunnel (represented by the distance from the face normalized by the tunnel radius; $D_{face}/R_{tunnel} = 0$ is the tunnel face, $D_{face}/R_{tunnel} > 0$ is ahead of the tunnel face and $D_{face}/R_{tunnel} < 0$ is behind the tunnel face). The displacements profiles are similar to each other, showing that the recommendations reached with a hydrostatic far-field stresses can be used for anisotropic geostatic stresses. This observation is supported by the results shown in Fig. 24, which is a plot of the principal stresses obtained from both models. As one can see, the results are similar.

It is worth mentioning that the reference 3D model has 326,906 nodes and requires 40 excavation steps, taking 13.46 h to run, while the recommended model has 51,246 nodes and 14 excavation steps, taking only 0.29 h to complete. That is, the recommended model runs almost 50 times faster than the reference model and provides equivalent results. Both models were run on the same computer (32 Gb RAM and Xeon E5-1660 v4, with 3.2 GHz processor).

Conclusions

In this paper, aspects that affect the 3D modelling of tunnels such as model size (width and length), grid refinement (transversal and longitudinal), grid type (structured and unstructured) and order of elements (i.e. interpolation

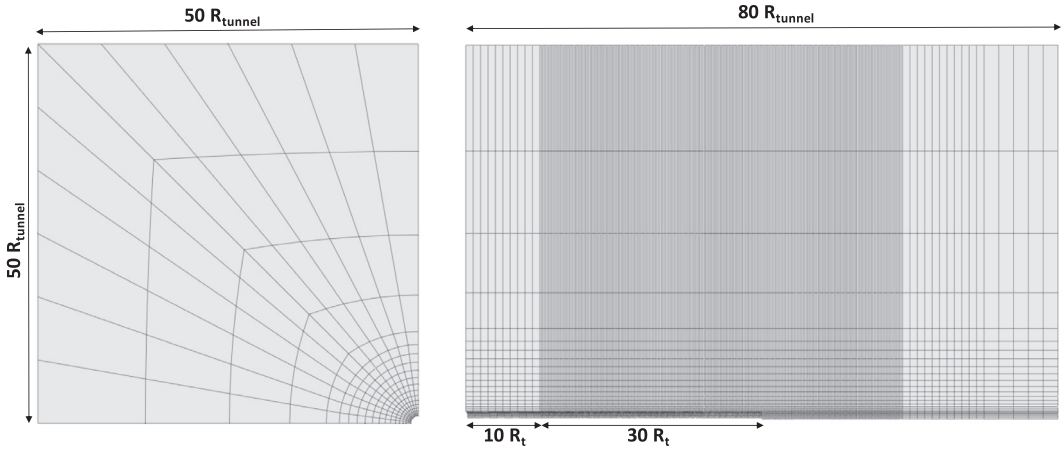

Fig. 21. Front and side view of the reference 3D model.

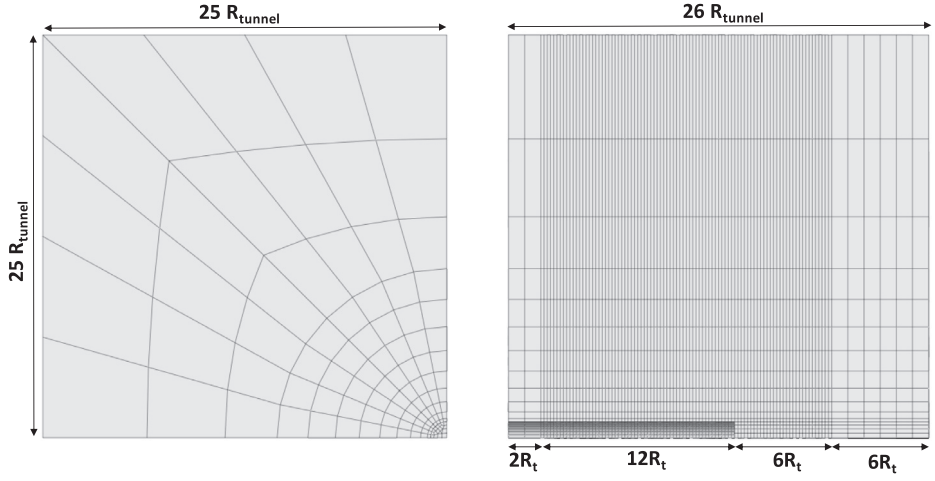

Fig. 22. Front and side view of the recommended 3D model, which dimensions and grid were determined based on the recommendations provided.

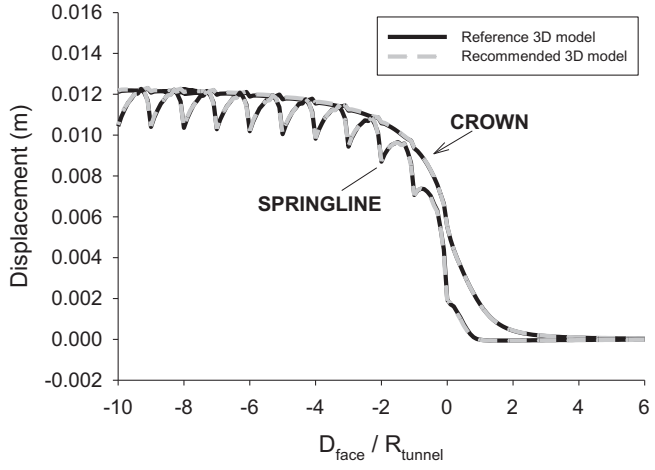

Fig. 23. Radial displacements at the wall and crown of the opening obtained with the reference and the recommended 3D models.

functions) are investigated, to provide recommendations for 3D meshing of FEM simulations of deep tunnels.

Finite element grids with 2nd order elements (i.e. quadratic interpolation) show better performance than finite element grids using 1st order elements (i.e. linear interpolation) when material nonlinearity is involved. Therefore, 2nd order elements should be preferred. Also, the structure of the grid (structured or unstructured grid) has a secondary importance compared with the order of the elements.

The size of the plastic zone has a major influence on the model dimensions. Requirements for model widths have been determined for yield radii (R_{yield}) varying from 1 (linear material) to 3 (worst case scenario). To achieve a 1% accuracy, for $R_{yield} = 3R_{tunnel}$ and associated flow rule, a model width of $32R_{tunnel}$ is required, while for $R_{yield} = 1R_{tunnel}$ (linear material), a width of $11R_{tunnel}$ is needed. This is in contrast with the common reference found in the literature of $10R_{tunnel}$, which may be suitable for a linear material but may not be acceptable for a nonlinear material.

Minimum model lengths have been also determined as a function of the yield radius. To obtain stresses and displacements with 1% accuracy, for $R_{yield} = 3R_{tunnel}$ and associated flow rule, the influence length of the excavation face is $23R_{tunnel}$ ($15R_{tunnel}$ behind the face

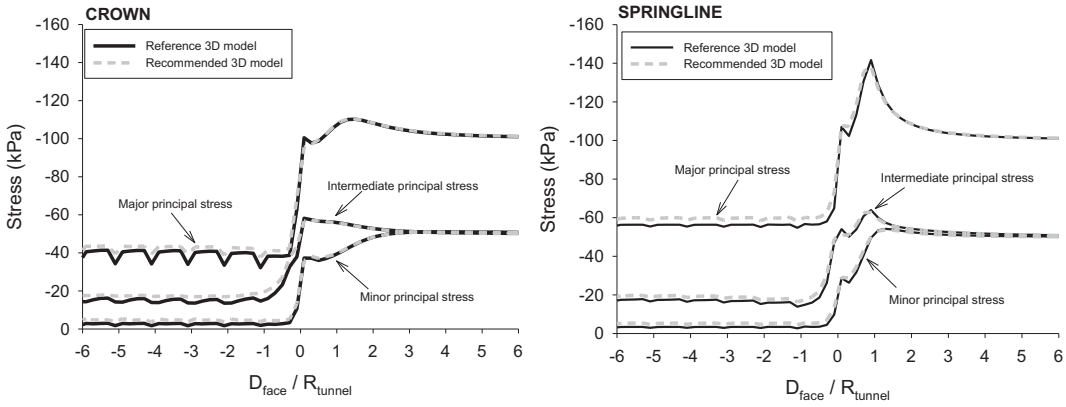

Fig. 24. Principal stresses at near the wall and crown of the opening obtained with the reference and the recommended 3D models.

and $8R_{tunnel}$ ahead), while for $R_{yield} = 1R_{tunnel}$ (linear material), the influence length is $9R_{tunnel}$ ($5R_{tunnel}$ behind and $4R_{tunnel}$ ahead). Common references found in the literature suggesting influence length of $4R_{tunnel}$ behind the face and $4R_{tunnel}$ ahead the face (e.g. Eberhardt, 2001, and Shahin, Nakai, Hinokio, & Yamaguchi, 2004) may be appropriate for linear materials, but can lead to unacceptable errors when a nonlinear material is involved. Further, the length affected by the front and back boundaries should be added to the model length. It is recommended to add $8R_{tunnel}$ to the length of influence of the excavation, $2R_{tunnel}$ from the front boundary and $6R_{tunnel}$ from the back boundary, to avoid boundary effects.

The paper also examines the minimum element length to be used when step-by-step excavation is attempted. This is necessary when an elastoplastic model is used, as the solution is stress-path dependent. Results from a number of simulations that explore the errors associated with different element sizes and excavation round lengths show that using 2nd order elements, with a maximum length of $0.2R_{tunnel}$, provides acceptable values for stresses and displacements.

While the recommendations provided have been found with the assumption of hydrostatic far-field initial stresses, additional cases using the suggested mesh dimensions with far-field anisotropic stresses indicate that the recommendations are also applicable to those cases with anisotropic far-field stresses.

The recommendations and conclusions reached with the work presented are not intended to cover all possible cases, as they have been obtained from a finite number of numerical experiments that, while covering a widespread of possibilities, are necessarily limited (e.g. they may not be applicable to shallow tunnels since they have not been included in the investigation). What is suggested should be taken as a first approximation for mesh optimization, while future work will, no doubt, refine and add to the recommendations.

Acknowledgments

The research is being partially supported by the research funding agency of Brazilian government CNPq (“Conselho Nacional de Desenvolvimento Cientifico”). The authors acknowledge the support from CNPq and also Midas company, which kindly provided the license of Midas GTX NX software, used in the present work.

References

Bobet, A. (2003). Effect of pore water pressure on tunnel support during static and seismic loading. *Tunnelling and Underground Space Technology, 18*(4), 377–393. https://doi.org/10.1016/S0886-7798(03)00008-7.

Cantieni, L., & Anagnostou, G. (2009). The effect of the stress path on squeezing behavior in tunneling. *Rock Mechanics and Rock Engineering, 42*(2), 289–318. https://doi.org/10.1007/s00603-008-0018-9.

Do, N. A., Dias, D., Oreste, P., & Djeran-Maigre, I. (2014). Three-dimensional numerical simulation of a mechanized twin tunnels in soft ground. *Tunnelling and Underground Space Technology, 42*, 40–51. https://doi.org/10.1016/j.tust.2014.02.001.

Eberhardt, E. (2001). Numerical modelling of three-dimension stress rotation ahead of an advancing tunnel face. *International Journal of Rock Mechanics and Mining Sciences, 38*(4), 499–518. https://doi.org/10.1016/S1365-1609(01)00017-X.

Franzius, J. N., & Potts, D. M. (2005). Influence of mesh geometry on three-dimensional finite-element analysis of tunnel excavation. *International Journal of Geomechanics, 5*(3), 256–266. https://doi.org/10.1061/(ASCE)1532-3641(2005) 5:3(256).

Gomes, R. a. M. P., & Celestino, T. B. (2009). Influence of physical and geometrical parameters on three-dimensional load transfer mechanism at tunnel face. *Canadian Geotechnical Journal, 46*(7), 855–868. https://doi.org/10.1139/T09-016.

Janin, J. P., Dias, D., Emeriault, F., Kastner, R., Le Bissonnais, H., & Guilloux, A. (2015). Numerical back-analysis of the southern Toulon tunnel measurements: A comparison of 3D and 2D approaches. *Engineering Geology, 195*, 42–52. https://doi.org/10.1016/j.enggeo.2015.04.028.

Mašín, D. (2009). 3D modelling of a NATM tunnel in high K_0 clay using two different constitutive models. *Journal of Geotechnical and Geoenvironmental Engineering ASCE, 135*(9), 1326–1335.

Meisnerr, H. (1996). Tunnelbau unter tage – Empfelunghen des Arbeitskreises. *Geotechnik, 19*(2), 99–108.

MIDAS Information Technology Co. (2014). Benchmarks & verification GTS NX manual.

Möller, S. (2006). *Tunnel induced settlements and structural forces in linings* PhD thesis. Stuttgart: Institute of Geotechnical Engineering, Universitat of Stuttgart.

Nam, S. W., & Bobet, A. (2007). Radial deformations induced by groundwater flow on deep circular tunnels. *Rock Mechanics and Rock Engineering, 40*(1), 23–39. https://doi.org/10.1007/s00603-006-0097-4.

Ng, C. W., & Lee, G. T. (2005). Three-dimensional ground settlements and stress-transfer mechanisms due to open-face tunnelling. *Canadian Geotechnical Journal, 42*(4), 1015–1029. https://doi.org/10.1139/t05-025.

Salesçon, J. (1969). Contraction Quasi-Statique D'une Cavite a Symetrie Spherique Ou Cylindrique Dans Un Milieu Elasto-Plastique. *Annales Des Ports Et Chaussees* (Vol. 4, pp. 231–236).

Shahin, H. M., Nakai, T., Hinokio, M., & Yamaguchi, D. (2004). 3D effects on earth pressure and displacements during tunnel excavations. *Soils and Foundations, 44*(5), 37–49.

Svoboda, T., & Masin, D. (2011). Comparison of displacement field predicted by 2D and 3D finite element modelling of shallow NATM tunnels in clays. *Geotechnik, 34*(2), 115–126. https://doi.org/10.1002/gete.201000009.

Vlachopoulos, N., & Diederichs, M. S. (2009). Improved longitudinal displacement profiles for convergence confinement analysis of deep tunnels. *Rock Mechanics and Rock Engineering, 42*(2), 131–146. https://doi.org/10.1007/s00603-009-0176-4.

Vlachopoulos, N., & Diederichs, M. S. (2014). Appropriate uses and practical limitations of 2D numerical analysis of tunnels and tunnel support response. *Geotechnical and Geological Engineering, 32*(2), 469–488. https://doi.org/10.1007/s10706-014-9727-x.

Yeo, C. H., Lee, F. H., Tan, S. C., Hasegawa, O., Suzuki, H., & Shinji, M. (2009). Three dimensional numerical modelling of a NATM tunnel. *Japanese Committee for Rock Mechanics, 5*(1), 33–38.